

The complex magnetic field topology of the cool Ap star 49 Cam

J. Silvester,¹★ O. Kochukhov,¹ N. Rusomarov¹ and G. A. Wade²

¹*Department of Astronomy and Space Physics, Uppsala University, SE-751 20 Uppsala, Sweden*

²*Department of Physics, Royal Military College of Canada, PO Box 17000, Station ‘Forces’, Kingston, ON K7K 7B4, Canada*

Accepted 2017 June 22. Received 2017 June 21; in original form 2017 April 6

ABSTRACT

49 Cam is a cool magnetic chemically peculiar star that has been noted for showing strong, complex Zeeman linear polarization signatures. This paper describes magnetic and chemical surface maps obtained for 49 Cam using the INVERS10 magnetic Doppler imaging code and high-resolution spectropolarimetric data in all four Stokes parameters collected with the ES-PaDOnS and Narval spectropolarimeters at the Canada–France–Hawaii Telescope and Pic du Midi Observatory. The reconstructed magnetic field maps of 49 Cam show a relatively complex structure. Describing the magnetic field topology in terms of spherical harmonics, we find significant contributions of modes up to $\ell = 3$, including toroidal components. Observations cannot be reproduced using a simple low-order multipolar magnetic field structure. 49 Cam exhibits a level of field complexity that has not been seen in magnetic maps of other cool Ap stars. Hence, we concluded that relatively complex magnetic fields are observed in Ap stars at both low and high effective temperatures. In addition to mapping the magnetic field, we also derive surface abundance distributions of nine chemical elements, including Ca, Sc, Ti, Cr, Fe, Ce, Pr, Nd and Eu. Comparing these abundance maps with the reconstructed magnetic field geometry, we find no clear relationship of the abundance distributions with the magnetic field for some elements. However, for other elements some distinct patterns are found. We discuss these results in the context of other recent magnetic mapping studies and theoretical predictions of radiative diffusion.

Key words: stars: chemically peculiar – stars: individual: 49 Cam – stars: magnetic field.

1 INTRODUCTION

The intermediate-mass Ap/Bp stars are A- and B-type main-sequence stars that display peculiar surface abundance patterns when compared to solar abundances. These abundance peculiarities are typically associated with a strong, global and stable magnetic field. These fields have strengths ranging from hundreds of gauss up to tens of kilogauss. Historically, the magnetic topologies of Ap/Bp stars have been considered to be close to a simple dipolar structure, but more recently it has been shown that the surface fields of some stars also contain significant contributions from complex substructures superimposed on a strong quasi-dipolar component (e.g. Kochukhov & Wade 2010). The observed peculiar abundances and abundance structures are thought to be a result of the build-up of chemical stratification in the radiative stellar envelope under the influence of radiative levitation and gravitational settling, mediated by the magnetic field and mixing processes (Michaud, Alecian & Richer 2015).

The standard phenomenological model for describing the variability of Ap/Bp stars is the oblique rotator model (Stibbs 1950),

which describes a rotating star whose magnetic axis is inclined relative to its rotational axis. By exploiting the rotation of these objects, Ap/Bp stars are often studied using Doppler imaging techniques for the purpose of reconstructing a two-dimensional surface map of chemical and magnetic field structures using spectroscopic or spectropolarimetric time-series observations (Kochukhov 2016).

The magnetic field geometry and the geometry of the chemical surface inhomogeneities at the surfaces of Ap/Bp stars give a key insight into the physical mechanisms governing the global magnetic field evolution in stellar interiors (Braithwaite & Nordlund 2006; Duez & Mathis 2010). By studying the magnetic field and chemical spots in detail, we can obtain empirical constraints on both the geometry of the field for theoretical modelling of the magnetized stellar interiors (e.g. Braithwaite & Nordlund 2006; Duez, Braithwaite & Mathis 2010) and for testing theories of atomic diffusion, thought to be responsible for the formation of chemical abundance inhomogeneities (e.g. Alecian 2015).

The Ap star 49 Cam (HD 62140) was classified as F0p (SrEu) by Cowley (1968) and later as A8p (SrEu) by Leone, Catanzaro & Catalano (2000a). An early detailed study of 49 Cam was carried out by Bonsack, Pilachowski & Wolff (1974), who examined the photometric and spectroscopic variations of this star. Later, a detailed analysis of the magnetic field geometry was performed

* E-mail: james.silvester@physics.uu.se

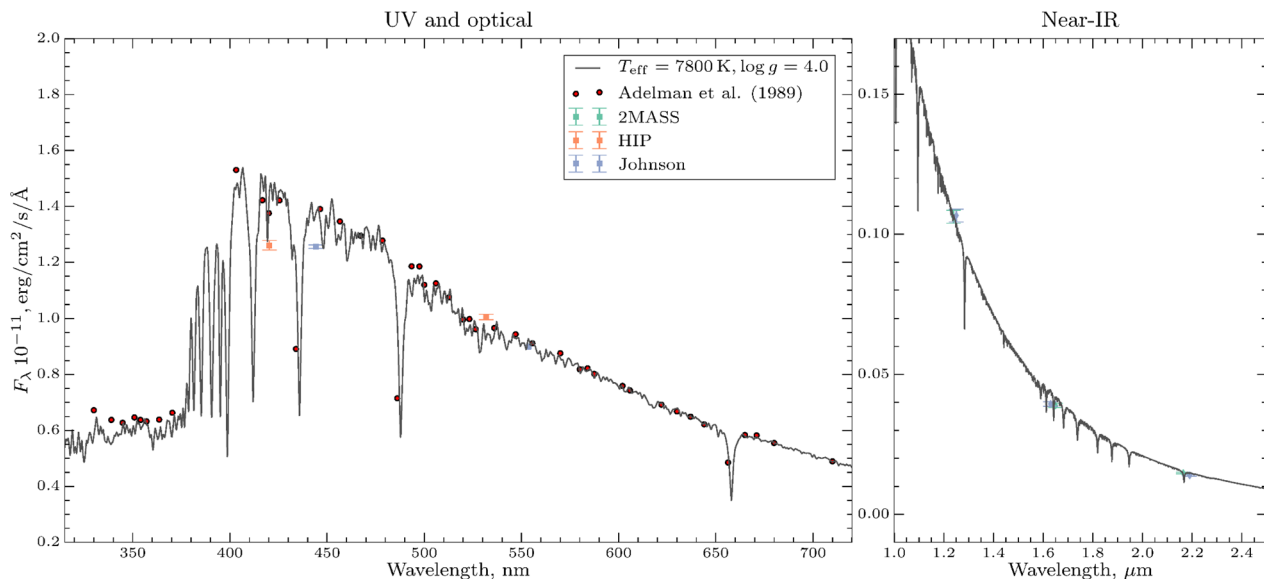


Figure 1. Comparison between theoretical spectral energy distribution (solid line) and observations (symbols) in the near-UV, optical and near-IR spectral regions. The theoretical SED corresponds to the calculations for $T_{\text{eff}} = 7800$ K and $\log g = 4.0$, including the effects of individual non-solar abundances and magnetic field.

by Leroy, Landstreet & Bagnulo (1994) and Leroy, Landolfi & Landi Degl’Innocenti (1996) using broad-band linear polarization measurements. 49 Cam was found to exhibit very strong linear polarization signatures by Leroy et al. (1994), who also demonstrated that the surface magnetic field of this star could not be described with a simple dipolar configuration. This work was an early indication of the complex field structure of 49 Cam and is a principal reason for including this star in our magnetic mapping programme.

High-resolution spectropolarimetric observations of 49 Cam have been obtained in Stokes *IQUV* on two occasions: first by Wade et al. (2000) and then by Silvester et al. (2012) as part of the data set obtained with the ESPaDOnS and Narval spectropolarimeters. In this paper, we use the Stokes parameter spectra collected by Silvester et al. (2012) to derive the magnetic and chemical maps of 49 Cam. This spectropolarimetric data set and similar data sets from the HARPSpol instrument at the ESO 3.6-m telescope have been successfully used for mapping the magnetic fields of a growing number of Ap stars, e.g. HD 32633 (Silvester, Kochukhov & Wade 2015), α^2 CVn (Silvester, Kochukhov & Wade 2014a,b), HD 24712 (Rusomarov et al. 2015) and HD 125248 (Rusomarov et al. 2016). These magnetic mapping studies have relied on using the magnetic Doppler imaging (MDI) inversion code *INVERS10* (Piskunov & Kochukhov 2002; Kochukhov & Piskunov 2002) that models four Stokes parameter line profiles with detailed polarized radiative transfer calculations and can simultaneously reconstruct the surface vector magnetic field maps and chemical abundance distributions. These MDI studies indicate that many Ap/Bp stars when modelled using four Stokes parameter data sets have magnetic fields that deviate from a low-order multipolar configuration and, especially, cannot be represented as oblique dipoles. For a complete list of Ap/Bp stars studied with the Doppler or magnetic Doppler imaging techniques, we refer to Kochukhov (2017); this paper also provides a series of tests of the reliability of chemical abundance maps reconstructed with *INVERS10*.

This paper is organized as follows. Section 2 briefly describes the observational data. In Section 3, the derivation of stellar parameters is discussed. In Section 4, the procedure for magnetic Doppler imaging is described. In Sections 5 and 6, the final magnetic field

map and chemical abundance maps are presented, respectively. The results and implications of this work are discussed in Section 7.

2 SPECTROPOLARIMETRIC OBSERVATIONS

Observations of 49 Cam analysed in this paper were obtained between 2006 and 2010, with both the ESPaDOnS and Narval spectropolarimeters. A detailed discussion of these observations, instruments, observing procedures and all essential aspects of data reduction is provided by Silvester et al. (2012). In total, 19 Stokes *IQUV* observations of 49 Cam are available. The spectra have a resolving power of 65 000, cover the wavelength range of 369–1048 nm and have a typical signal-to-noise ratio of 600:1.

3 STELLAR PARAMETERS

49 Cam is a fairly broad-lined Ap star with an effective temperature in the range 7700–8000 K (Adelman 1982; Babel 1994; Ryabchikova et al. 2001). We re-determined the stellar effective temperature by computing a small grid (with steps of 50 K) of model atmospheres within the range of T_{eff} reported in the literature using the *LLMODELS* code (Shulyak et al. 2004) and comparing the resulting theoretical spectral energy distributions (SEDs) with the observations in the optical (Johnson and *Hipparcos* photometry converted to absolute fluxes and spectrophotometry by Adelman et al. (1989)) and near-IR (2MASS fluxes) wavelength regions. The formulas of Lipski & Stępień (2008) were used to convert the Adelman magnitudes to fluxes. The 2MASS observations were converted using formulas from Cohen, Wheaton & Megeath (2003) and the calibration for Johnson photometry by Bessell, Castelli & Plez (1998) was used.

According to the literature, 49 Cam is not significantly reddened (e.g. Adelman 1982), so reddening was not included in the calculations. The temperature was selected by the evaluation of the model that gave the best fit (by visual inspection) between the model flux distributions and the observational data. The best fit was obtained for $T_{\text{eff}} = 7800$ K. The corresponding comparison between the observed and theoretical SED is shown in Fig. 1. Following the same

Table 1. Parameters of 49 Cam.

Parameter	Value	Reference
T_{eff}	7800 ± 200 K	This study
$\log g$	4.00 ± 0.25	This study
P_{rot}	4.28679 d	Adelman (1997)
R	$2.25 \pm 0.25 R_{\odot}$	This study
$v \sin i$	23.0 ± 1.0 km s ⁻¹	This study
i	$120 \pm 10^{\circ}$	This study
Θ	$40 \pm 5^{\circ}$	This study

procedure, we examined a series of SEDs for model atmospheres with different values of $\log g$ (each varying by a step of 0.25) and found that $\log g = 4.0$ gave the best fit to observations. An uncertainty of 0.25 is assigned based on the step between different $\log g$ values tested. Therefore, we adopted $T_{\text{eff}} = 7800$ K and $\log g = 4.0$ for the subsequent analysis of 49 Cam.

The LLMODELS model atmosphere calculations took into account individual stellar abundances for about a dozen chemical species, including Fe peak and several rare-earth elements. These abundances were determined by fitting the SYNMAST (Kochukhov, Makaganiuk & Piskunov 2010) theoretical spectra to observations of 49 Cam based on an initial solar abundance model. The model atmosphere calculations also incorporated a modification of the line opacity due to Zeeman splitting and polarized radiative transfer (Khan & Shulyak 2006). For these calculations, we assumed a magnetic field modulus of 3 kG (Glagolevskij 2011).

An initial estimate of the projected rotational velocity $v \sin i$ was obtained by fitting a selection of spectral lines, typically in the 4500–5000 Å wavelength region, with a synthetic spectrum. The projected rotational velocity was found to be 23 ± 1 km s⁻¹, in agreement with the value reported by Silvester et al. (2012).

As a by-product of matching theoretical SEDs to observations, we derived an angular diameter that can be converted to the stellar radius, $R = 2.25 \pm 0.25 R_{\odot}$, for the parallax $\pi = 10.34 \pm 0.45$ mas (van Leeuwen 2007). Our radius value agrees well with the previous estimate by Kochukhov & Bagnulo (2006, $2.11 R_{\odot}$), but is marginally inconsistent with $R = 1.9 R_{\odot}$ given by Leone, Catanzaro & Catalano (2000b). The radius uncertainty is calculated based on the parallax uncertainty and the uncertainty from the derived angular diameter.

Rotational phases of observations were calculated according to the ephemeris by Adelman (1997): $\text{JD} = 2441257.300 + 4^{\text{d}}28679 \cdot E$. The summary of derived stellar parameters for 49 Cam in this paper or adopted from the literature is given in Table 1.

4 MAGNETIC MAPPING AND CHEMICAL INVERSIONS

To reconstruct the magnetic field of 49 Cam, we performed inversions of Stokes $IQUV$ profiles using INVERS10 (Piskunov & Kochukhov 2002). The magnetic Doppler imaging in this study very closely follows the methodology used in our previous mapping of the Ap stars α^2 CVn (Silvester et al. 2014a,b) and HD 32633 (Silvester et al. 2015).

Within the inversion code, the magnetic field topology is parametrized in terms of a general spherical harmonic expansion (up to the angular degree $\ell = 10$ in this study) as described by Kochukhov et al. (2014). To facilitate convergence to a global chi-square minimum, a regularization function is used. In the case of spherical harmonics, the regulation function acts to limit the field

structure to the simplest harmonic distribution that provides a satisfactory fit to the data.

The regularization was chosen by a stepwise approach, with each successive step of decreasing levels of regularization. Following the methodology described by Kochukhov (2017), the final value of regularization was chosen at the point in which the fit between the observations and the model was no longer significantly improved by decreasing regularization. Typically, we choose a value of 2–5 for the ratio of the total deviation to the total regularization. This approach was used both for the magnetic and abundance maps.

The field reconstruction requires knowledge of several stellar properties. The projected rotational velocity ($v \sin i$) and the inclination (i , which is the angle between the rotational axis and the line of sight) must be known. In addition, modelling of the Stokes QU observations requires knowledge of the azimuth angle (Θ) of the stellar rotational axis. To verify our initial determination of $v \sin i$, we performed an additional series of test inversions with different $v \sin i$ values and confirmed that a $v \sin i$ of 23 km s⁻¹ did result in the smallest deviation between the model spectra and the observations.

To determine an inclination angle, we considered values reported for 49 Cam in the literature, such as 61° given by Stepien (1989) and 90° used by Leroy et al. (1996). We produced a grid of inversions with i covering this range and selected the value that gave the smallest deviation between the model spectra and the observations. As a result of this procedure, we initially found the best-fitting inclination $i = 60^{\circ}$, which also agreed with the inclination angle that follows from the stellar $v \sin i$, radius and rotational period. However, for any given derived inclination angle, $i = 180^{\circ} - i$ is also a possible alternative solution. To check which of the two possible solutions gave the best fit, inversions were also performed for $i = 180^{\circ} - 60^{\circ} = 120^{\circ}$. We found that $i = 120^{\circ}$ gave a slightly improved fit to the data and we therefore adopted that as our final value $i = 120^{\circ} \pm 10^{\circ}$. It should be noted that we do not find large differences between the final $i = 60^{\circ}$ and $i = 120^{\circ}$ maps, thus either option gives comparable results.

As discussed by Kochukhov et al. (2004), an uncertainty of 10° in the inclination angle is deemed to have little effect on the resulting maps. A Θ angle of 20° was also determined on the basis of a similar grid inversion approach.

5 MAGNETIC FIELD STRUCTURE

The final magnetic field map for 49 Cam was derived using a set of Stokes $IQUV$ profiles for Ti, Cr, Fe and Nd lines. These lines were selected on the basis that they contain no significant blends and that they exhibited strong polarization signatures. For the magnetic mapping, all the lines selected were modelled simultaneously and the chemical abundance distribution maps for those elements were also derived simultaneously. The relative weights of the Stokes $IQUV$ contributions are determined and assigned automatically by the code.

Information on atomic parameters of these lines is given in Table 2. The resulting magnetic field map is presented in Fig. 2. For comparison, we also derived the magnetic field ignoring information in the Stokes QU profiles. This magnetic map is shown in Fig. 3. The fits between the model profiles and the observed profiles are illustrated in Figs 4–7. It should be noted that a limited number of Stokes QU profiles are poorly fit at certain phases. However, these poorly fit profiles are limited to stronger lines and thus this suggests that this discrepancy is likely due to the chemical stratification of these elements. This phenomenon is well known to occur in cooler Ap stars such as 49 Cam and is not taken into account in the

Table 2. Atomic lines used for the mapping of 49 Cam. The $\log gf$ values are adopted from the VALD3 data base (Ryabchikova et al. 2015).

Ion	Wavelength (Å)	$\log gf$
Magnetic and abundance mapping		
Ti II	4394.059	-1.770
	4395.031	-0.540
	4779.985	-1.260
Cr II	4588.199	-0.627
	4812.337	-1.960
	5407.604	-2.151
Fe II	4620.513	-3.240
	4923.927	-1.320
	5018.440	-1.220
	5169.033	-1.303
Fe I	6230.722	-1.281
Nd III	5050.695	-1.060
	5429.794	-1.240
	5677.178	-1.450
	5851.542	-1.550
Abundance mapping		
Ca I	6122.217	-0.316
	6162.173	-0.090
Sc II	5526.790	0.024
Ce II	4562.359	0.210
Pr III	7030.386	-0.929
Eu II	6437.631	-0.602
	6645.094	-0.162

inversion code. There are some limited instances where overfits to the Stokes QU profiles are seen (e.g. for the phases of 0.677 and 0.681 in Nd 3 lines). To get the best representation of the magnetic field, the field is derived using as many elements as possible. This will in some cases result in a small number of overfitted or underfitted regions. This is an unavoidable consequence of using many lines, and it should be noted however that in the case of the overfit to these discrete Nd profiles, the overall contribution to the final magnetic field derived is negligible.

The magnetic field of 49 Cam shows a relatively complex structure. In particular, the field topology of this star is considerably more complex than that of HD 24712 (Rusomarov et al. 2015), which is the only other cool Ap star mapped using line profiles in all four Stokes parameters. Contributions of different harmonic terms to the field topology are reported in Table 3. Considering this table and Fig. 8, there is a significant contribution of the $\ell = 1, 2$ harmonic modes and large contributions of the $\ell = 3, 4$ modes. This is reflected in the complex nature of the vector magnetic field map as presented in Fig. 2, which shows two structures near the stellar equator (seen clearly at phases 0.20 and 0.80). These regions also correspond to the large horizontal field structures seen, for example at a phase of 0.20.

To test the reliability of magnetic maps and to verify the complexity of the field, inversions were performed with the maximum angular degree of spherical harmonics limited to $\ell = 2$, thus forcing the field to remain simple in structure. In the resulting inversions, both Stokes Q and U profiles were extremely poorly fit, as can be

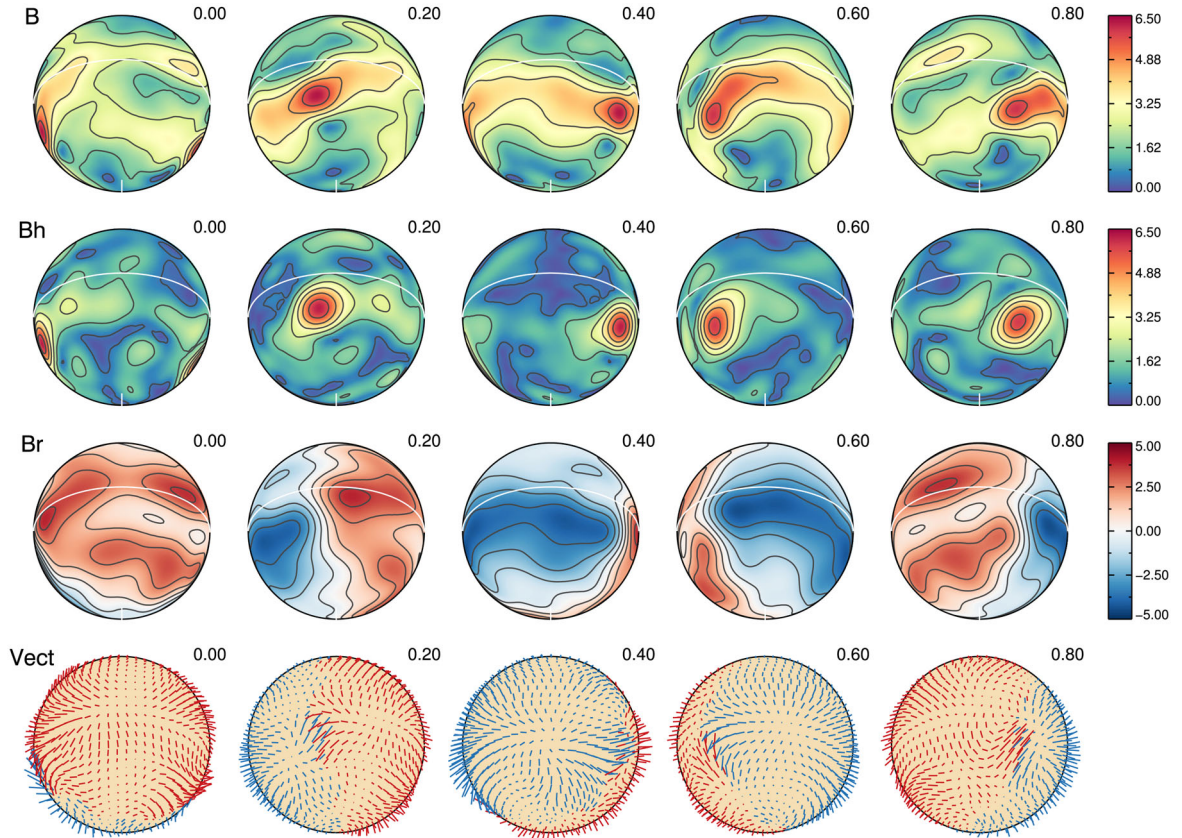


Figure 2. Surface magnetic field distribution of 49 Cam derived using Stokes $IQUV$ profiles. The spherical plots, displayed at the inclination angle of $i = 120^\circ$, show distributions of the field modulus, horizontal field, the radial field and the field orientation. Each column corresponds to a different phase of rotation (0.0, 0.2, 0.4, 0.6 and 0.8) and the colour bars on the right side indicate the magnetic field strength in kG. The contours over the top three maps are plotted with a 1.0 kG step.

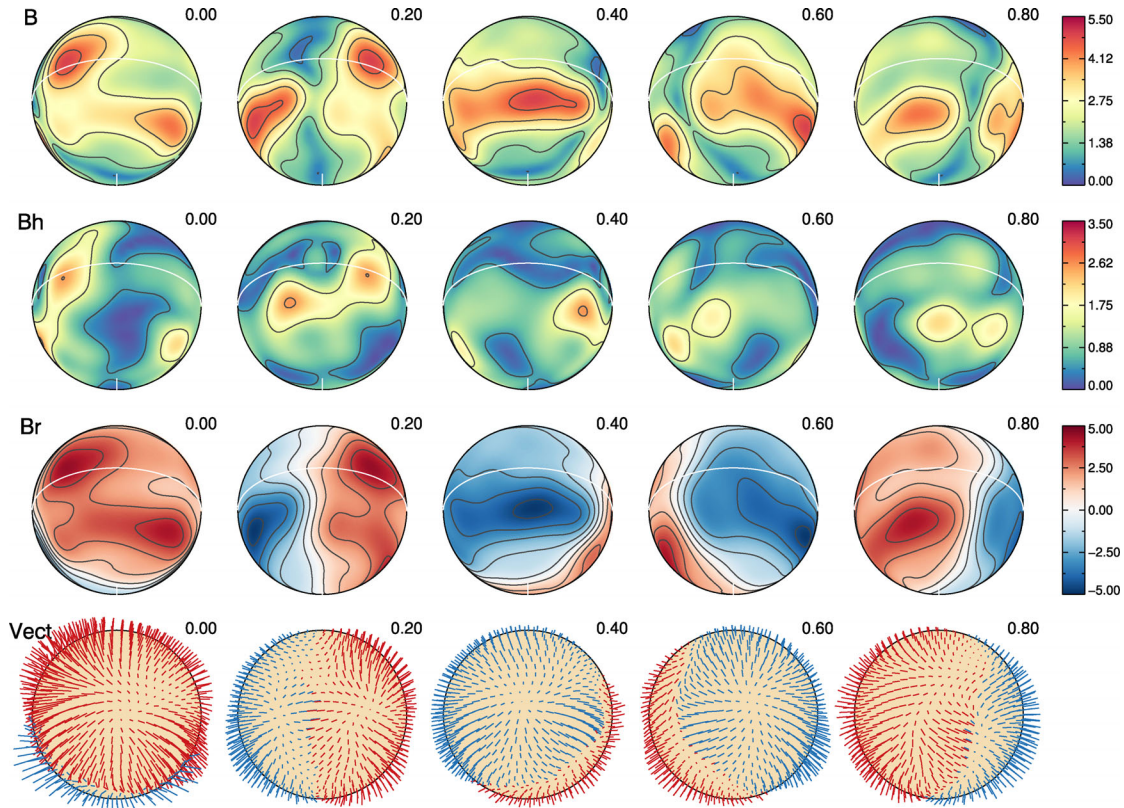


Figure 3. Same as Fig. 2 but for the surface magnetic field distribution reconstructed using Stokes *IV* spectra.

seen from Figs 4–7. This strongly indicates that the magnetic field of 49 Cam cannot be described with a superposition of simple dipole and quadrupole components.

An important related test that we have conducted was an assessment of the contribution of information in the linear polarization (Stokes *QU*) profiles to the magnetic inversion. To this end, we repeated inversions using only Stokes *I* and *V* observations. The resulting magnetic map is shown in Fig. 3 and the distribution of energies for the $\ell = 1$ –4 modes is given in Table 4. The magnetic field topology inferred from the modelling of the Stokes *IV* data is somewhat simplified compared to the outcome of the four Stokes parameter inversion. In particular, we note that the horizontal field is much weaker due to the absence of linear polarization information. However, we still find significant contributions of $\ell = 2$ and 3 harmonic modes.

Compared to the harmonic magnetic energy spectrum of both α^2 CVn (Silvester et al. 2014b) and HD 32633 (Silvester et al. 2015), the magnetic field of 49 Cam appears to be much more complex, with more energy in higher harmonic modes. In the case of these other stars, the harmonic energies were concentrated primarily to the first two modes with $\ell = 1, 2$, with higher ℓ contributions limited to few per cent. Another cool Ap star ($T_{\text{eff}} = 9850$ K) that has also shown some higher order complexity is CS Vir (Rusomarov et al. 2016) with a total $\ell = 3$ contribution of 8.9 per cent, which is only slightly more than one-half the $\ell = 3$ contribution of 49 Cam. Thus, 49 Cam remains the Ap star with the largest $\ell = 3$ contribution mapped to date.

6 CHEMICAL ABUNDANCE DISTRIBUTIONS

We selected chemical elements that need to be mapped using the same methodology as implemented by Silvester et al. (2014b) for

α^2 CVn and by Silvester et al. (2015) for HD 32633. Because of the lower effective temperature and the different abundance pattern of 49 Cam, combined with its significant $v \sin i$, many spectral lines are heavily blended and the abundance maps are thus necessarily based on a limited set of essentially unblended lines.

The final derived chemical abundance maps were produced using either inversions where the abundance distributions were derived simultaneously with the magnetic field using Stokes *IQUV* or Stokes *IV* observations, with the magnetic field used as a fixed input and with this field being derived from the full Stokes *IQUV* inversion. For 49 Cam, Ti, Cr, Fe and Nd were derived simultaneously with the magnetic field (and with Stokes *IQUV*) and Ca, Sc, Ce, Pr and Eu were derived with the fixed magnetic field (and from Stokes *IV*). The list of lines used for abundance DI mapping is given in Table 2.

For the final abundance spherical maps, an abundance scale was chosen such that extreme abundance value outliers were excluded from the final plot. The outliers normally comprised 2–12 per cent of all the surface elements and were selected with the use of a histogram plot: this was the same procedure as described by Silvester et al. (2014b, 2015).

6.1 Calcium and scandium

The calcium abundance map was reconstructed using the Stokes *IV* profiles of the Ca $\lambda\lambda$ 6122 and 6162 lines. The comparison of observations and the model profiles can be seen in Fig. 11 and the resulting map is presented in Fig. 9. The calcium abundance ranges from -3.5 to -7.0 dex in the $\log N_{\text{el}}/N_{\text{tot}}$ scale (the solar value is -5.70). There are distinct areas of enhancement localized to spot-like regions close to the stellar equator. The location of these distinct spots is difficult to clearly correlate with the magnetic field.

Stokes I

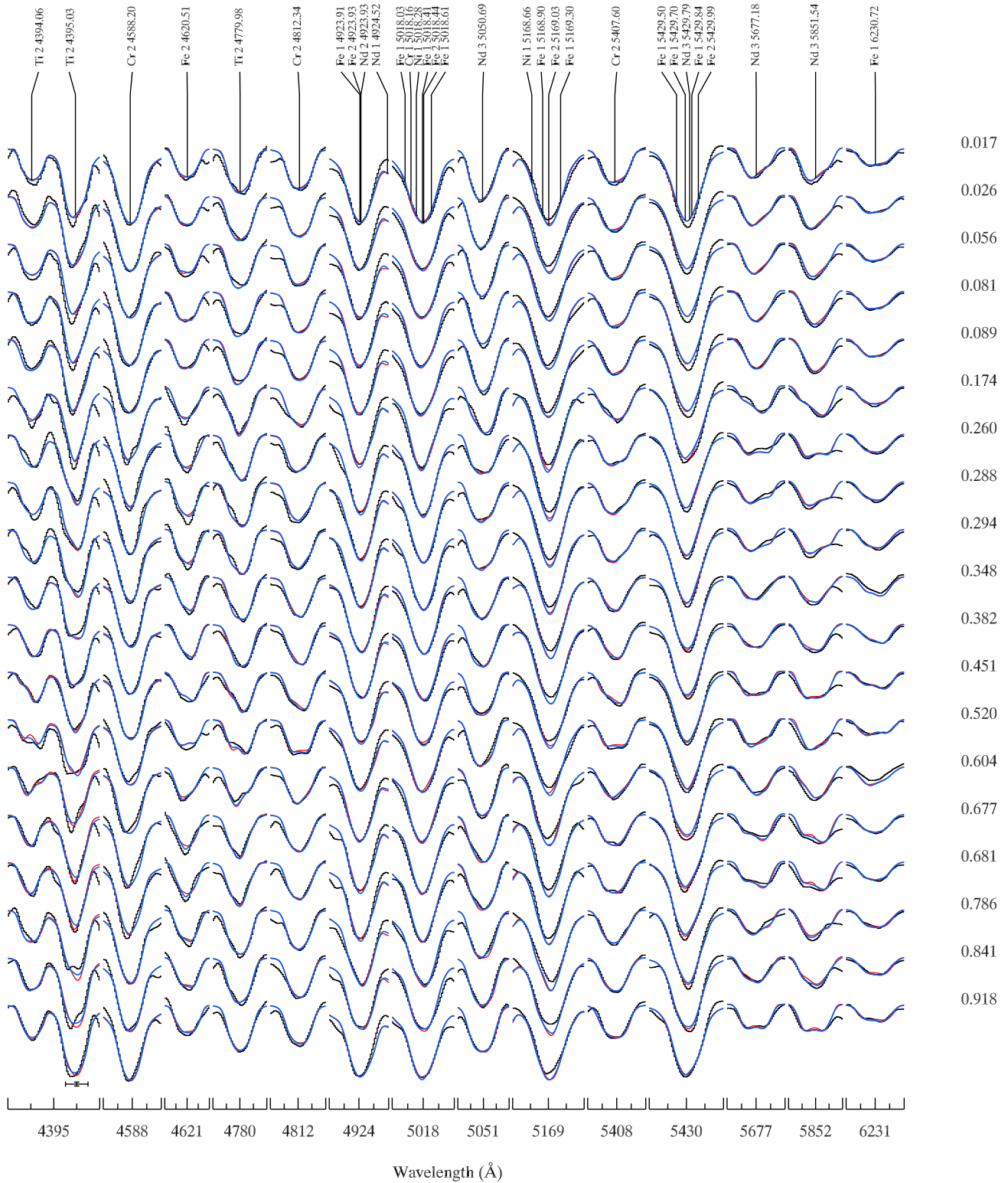


Figure 4. Stokes I profiles for all lines used in the magnetic field mapping. Observed spectra (black histogram line) are compared to the synthetic profiles corresponding to the general spherical harmonic inversion (thick blue lines) and to the inversion limited to $\ell = 2$ harmonic modes (thin red line). The spectra are offset vertically according to the rotational phase indicated to the right of the panel. The bars in the lower left corners indicate the vertical and horizontal scales (2 per cent of the Stokes I continuum intensity and 0.5 Å).

Stokes V

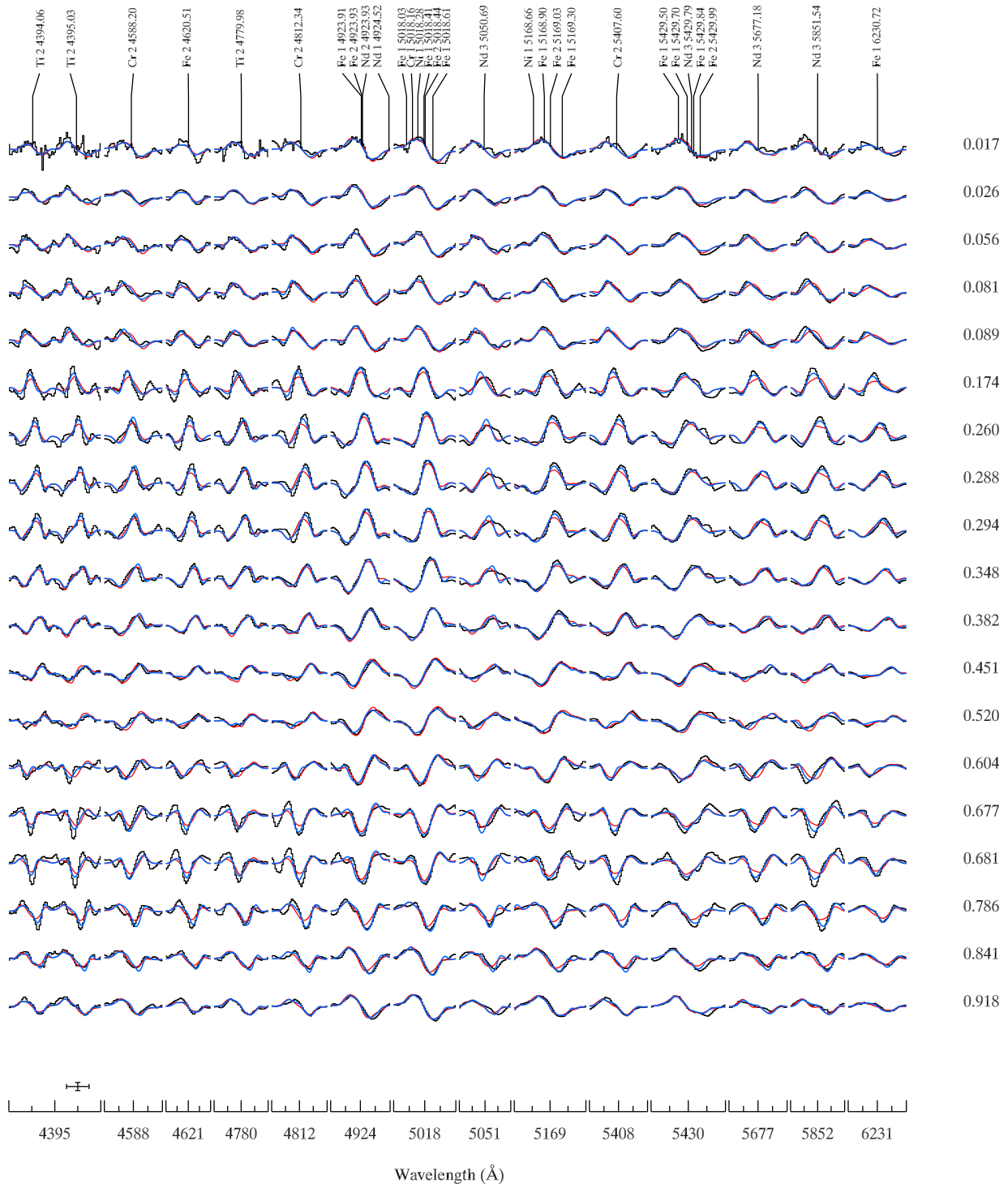


Figure 5. Same as Fig. 4 but for the Stokes V profiles.

The scandium abundance map was reconstructed using the Stokes IV profile of the Sc II λ 5526 line. The comparison of observations and the model profiles is shown in Fig. 11 and the resulting map is presented in Fig. 9. The scandium abundance ranges from -7.5 to -10.0 dex (the solar value is -8.89). Similar to

calcium, scandium is located in distinct areas of enhancement, larger in extent than what is seen for calcium. The enhancements are located predominantly near regions where the radial magnetic field component is weak and the horizontal component is strong.

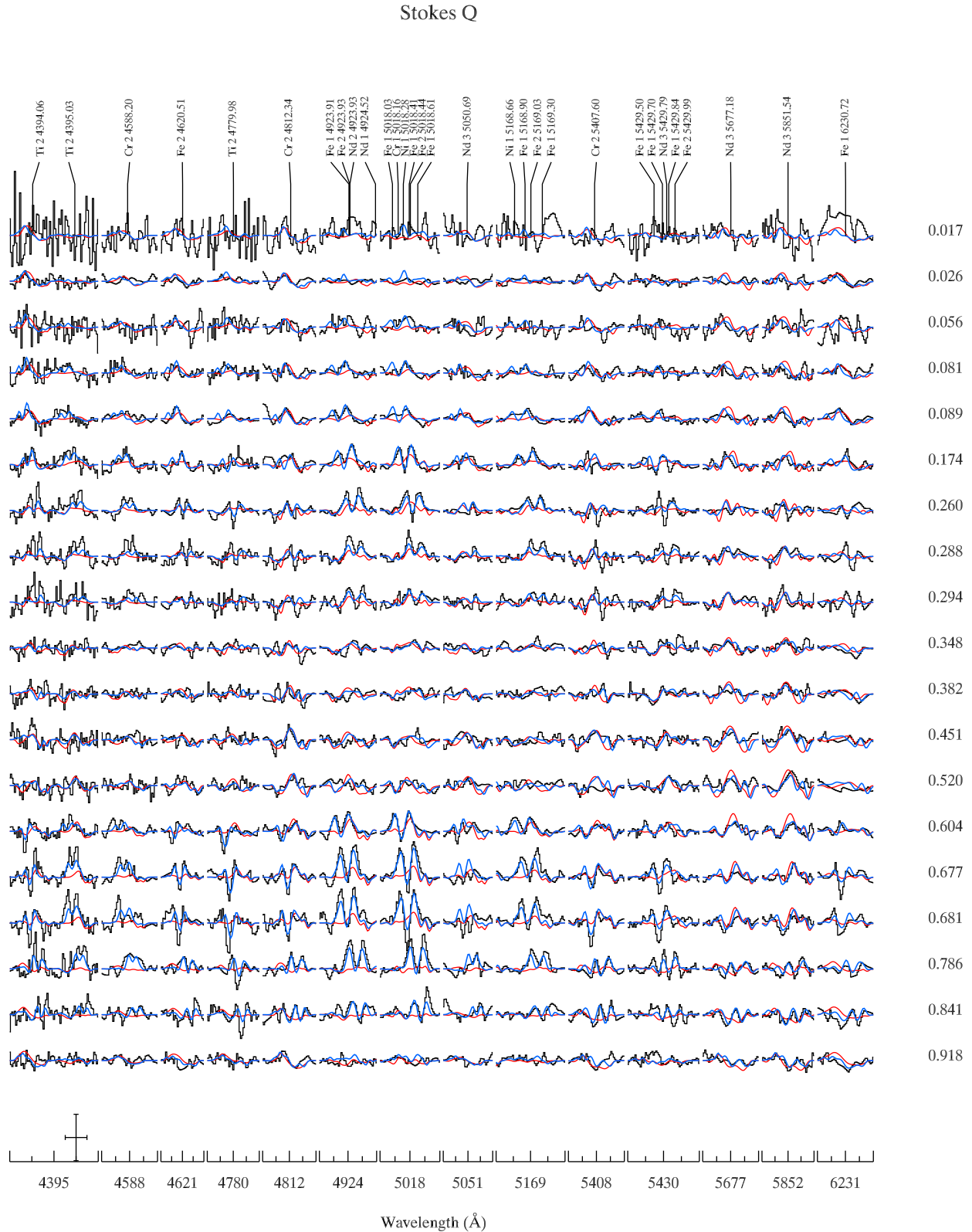


Figure 6. Same as Fig. 4 but for the Stokes Q profiles.

6.2 Titanium, chromium and iron

For titanium, the abundance map was produced from the Stokes $IQUV$ profiles of the Ti II $\lambda\lambda$ 4394, 4395 and 4779 lines. The resulting comparison between the observations and the model profiles

can be seen in Figs 4, 6, 7 and 5 and the resulting titanium distribution is given in Fig. 9. The titanium abundance ranges from -4.7 to -9.0 dex (the solar value is -7.09). The titanium abundance is characterized by a pattern of enhancements located only in the

Stokes U

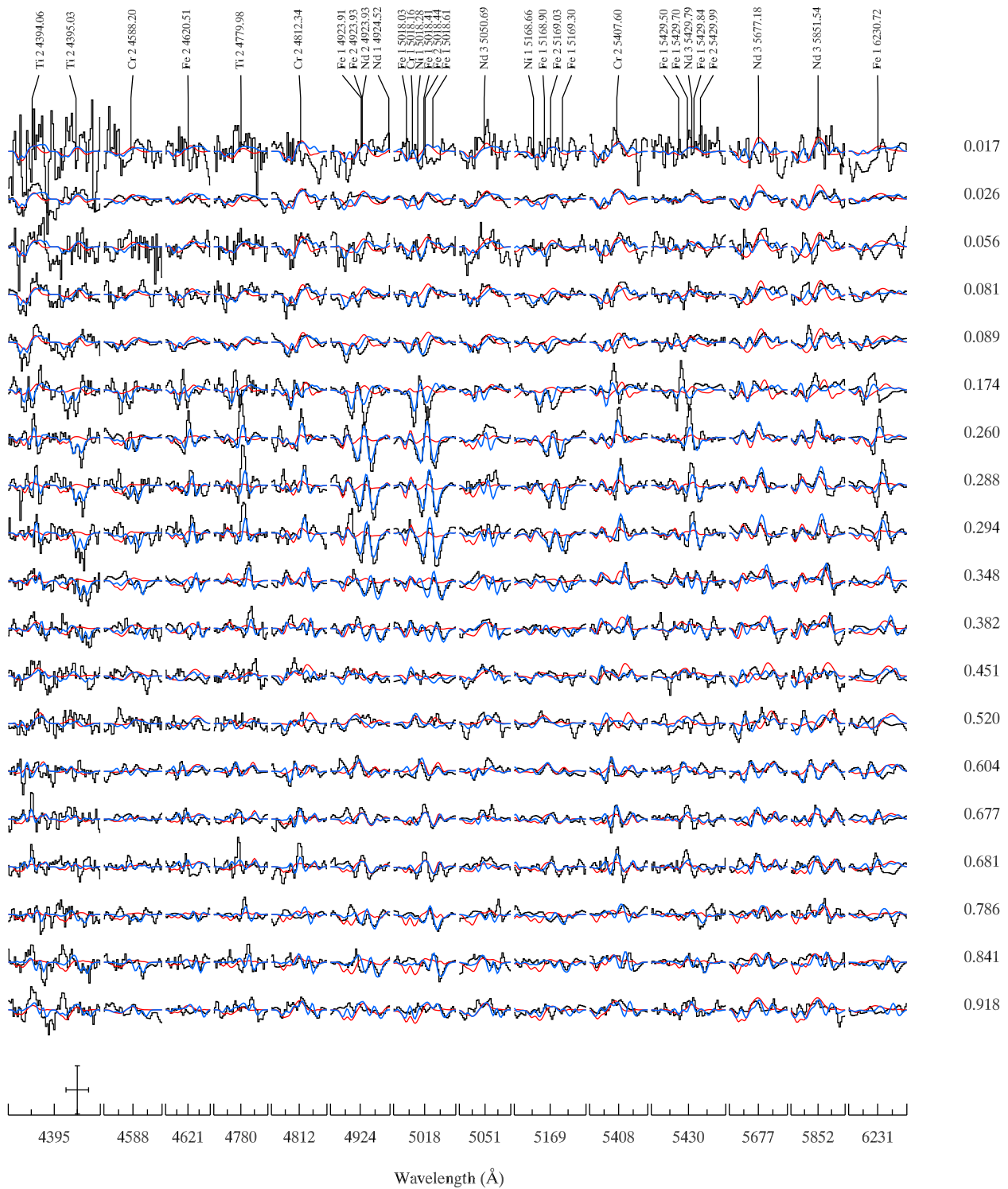


Figure 7. Same as Fig. 4 but for the Stokes *U* profiles.

Table 3. Distribution of the poloidal (E_{pol}) and toroidal (E_{tor}) magnetic field energy over different harmonic modes for the best-fitting Stokes $IQUV$ MDI map of 49 Cam.

ℓ	E_{pol} (per cent)	E_{tor} (per cent)	E_{tot} (per cent)
1	49.0	2.8	51.8
2	5.6	4.7	10.3
3	13.1	3.6	16.7
4	2.1	3.0	4.9
5	3.6	1.6	5.2
6	2.4	1.6	4.0
7	1.2	1.3	2.5
8	1.1	0.7	1.8
9	0.7	0.5	1.2
10	1.1	0.4	1.5
Total	79.7	20.3	100

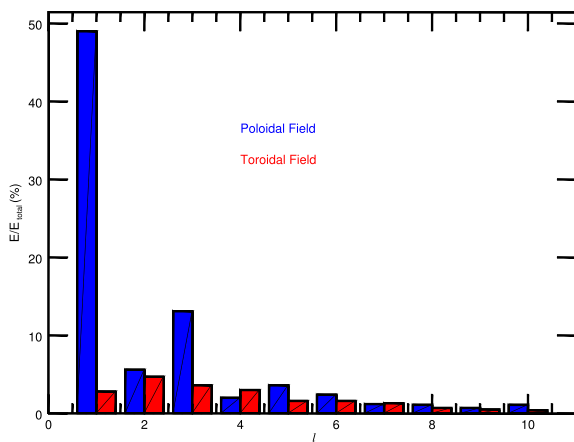


Figure 8. Distribution of the magnetic energy between different spherical harmonic modes in the MDI magnetic field map of 49 Cam. Bars of different colours represent the poloidal (blue/dark) and toroidal (red/light) magnetic components.

Table 4. Distribution of the poloidal (E_{pol}) and toroidal (E_{tor}) magnetic field energy truncated for the first four harmonics for the Stokes IV -only fit.

ℓ	E_{pol} (per cent)	E_{tor} (per cent)	E_{tot} (per cent)
1	74.7	1.9	76.6
2	5.6	1.8	7.3
3	6.5	2.2	8.7
4	1.1	1.1	2.2

bottom hemisphere, with a depleted area in the lower hemisphere. The areas of enhancement do not appear to strongly correlate with the magnetic field.

A chromium map was reconstructed using the Stokes $IQUV$ profiles of the Cr II $\lambda\lambda$ 4588, 4812 and 5407 lines. The fit between observations and the model profiles is shown in Figs 4, 6, 7 and 5. The corresponding chromium distribution is displayed in Fig. 9. The chromium abundance ranges from -2.5 to -6.0 dex (the solar value is -6.40). The largest chromium overabundance regions are located in the upper hemisphere. No clear correlations between the magnetic field structure and the Cr abundance map are evident.

The iron map was reconstructed from the Stokes $IQUV$ profiles of the Fe II $\lambda\lambda$ 4620, 4923, 5018, 5169 and Fe I λ 6230 lines. The final fit between the observed and synthetic spectra is shown in Figs 4, 6, 7 and 5, with the resulting iron distribution given in Fig. 9. The abundance range for iron is from -2.5 to -7.0 dex (the solar value is -4.54). The iron abundance forms a very distinct ring of enhancement in the lower hemisphere around the area where the radial magnetic field is relatively high. This enhancement ring is broken at the location of the strong horizontal magnetic field patch near the magnetic equator.

6.3 Cerium and praseodymium

The cerium abundance map was reconstructed using the Stokes IV profiles of the Ce II λ 4562 line. The comparison of observations and the model profiles can be seen in Fig. 11 and the resulting map is presented in Fig. 10. The cerium abundance ranges from -7.5 to -10.5 dex (the solar value is -10.46). The cerium abundance distribution has large areas of enhancement and depletion. Comparing to the magnetic field, no clear correlations could be identified.

The praseodymium chemical map was reconstructed using the Stokes IV profile of the Pr III λ 7030 line. The comparison of observations and the model profiles can be seen in Fig. 11 and the resulting map is presented in Fig. 10. The praseodymium abundance ranges from -5.0 to -9.0 dex (the solar value is -11.32). The praseodymium abundance distribution has distinct spots with large areas of relative overabundance. These enhancements seem to be associated with the areas of a strong radial magnetic field component. The areas of relative depletion seem to be located where the radial field is weak and the horizontal field is strong.

6.4 Neodymium and europium

Neodymium was reconstructed using the Stokes $IQUV$ spectra of Nd III $\lambda\lambda$ 5050, 5429, 5677 and 5851. The comparison between observations and the model profiles is shown in Figs 4, 6, 7 and 5. The resulting map is shown in Fig. 10. The neodymium abundance ranges from -5.5 to -8.5 dex (the solar value is -10.62). The neodymium distribution is a less extreme version of the praseodymium distribution, with the largest enhancements also seen in areas where the positive radial component is relatively strong. The areas of lowest abundance seem to be located at the magnetic equator, where the horizontal field reaches maximum.

The europium abundance map was reconstructed using the Stokes IV profiles of the Eu II $\lambda\lambda$ 6437 and 6645 lines. The comparison of observations and the model profiles can be seen in Fig. 11 and the resulting map is presented in Fig. 10. The europium abundance ranges from -5.0 to -10.0 dex (the solar value is -11.52). The europium distribution is similar to the praseodymium distribution, with areas of enhancement seen where the radial field is somewhat stronger and depleted areas near regions of weaker radial component and stronger horizontal field component. The europium lines used here have both hyperfine and isotopic structures, neither of which was included in our inversions. The same lines were used in Eu mapping for α^2 CVn (Silvester et al. 2014b) and it was verified that including their fine structure did not lead to an appreciable improvement in the fit quality or a change in the resulting abundance map.

7 CONCLUSION AND DISCUSSION

We have carried out a magnetic Doppler imaging modelling of the full Stokes vector, high-resolution observations of the cool Ap star

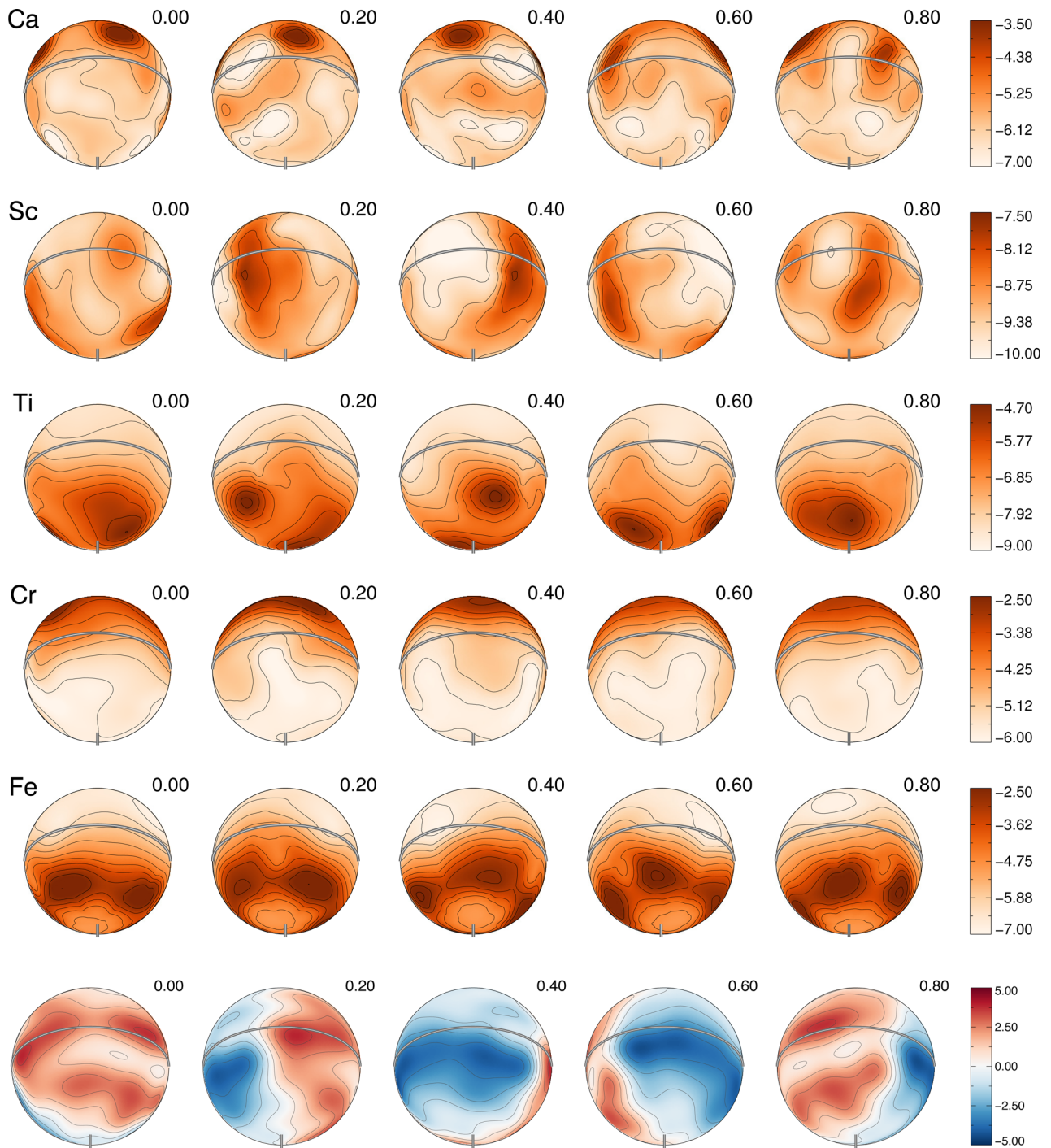


Figure 9. Chemical abundance distributions derived for Ca, Sc, Ti, Cr and Fe. Each column corresponds to a different rotational phase (0.0, 0.2, 0.4, 0.6 and 0.8). The solid line shows the location of the stellar equator. The visible rotational pole is indicated by the short thick line. The colour bars on the right side indicate chemical abundance in the $\log N_{el}/N_{tot}$ units. The abundance contours are plotted with a 0.5 dex step. The radial magnetic field from the Stokes $IQUV$ is shown in the bottom row for comparison.

49 Cam. This star is found to have a complex magnetic field structure combined with distinct abundance patterns. The magnetic field has significant contributions of the harmonic modes with ℓ up to 4, with a significant toroidal component. The necessity for such a complex field is supported by the fact that the observed Stokes $IQUV$ profiles cannot be reproduced by using a simpler field geometry and also by the relative complexity of the field structure inferred from the

Stokes IV inversions. The magnetic field of 49 Cam is significantly more complex than the fields of α^2 CVn and HD 32633 (Silvester et al. 2014b, 2015) mapped in four Stokes parameters using the comparable ESPaDOnS/Narval data set, and is dramatically more structured than the field of the cool Ap star HD 24712 studied with the HARPSpol Stokes $IQUV$ data (Rusomarov et al. 2015). Our conclusions are qualitatively consistent with those of Leroy et al.

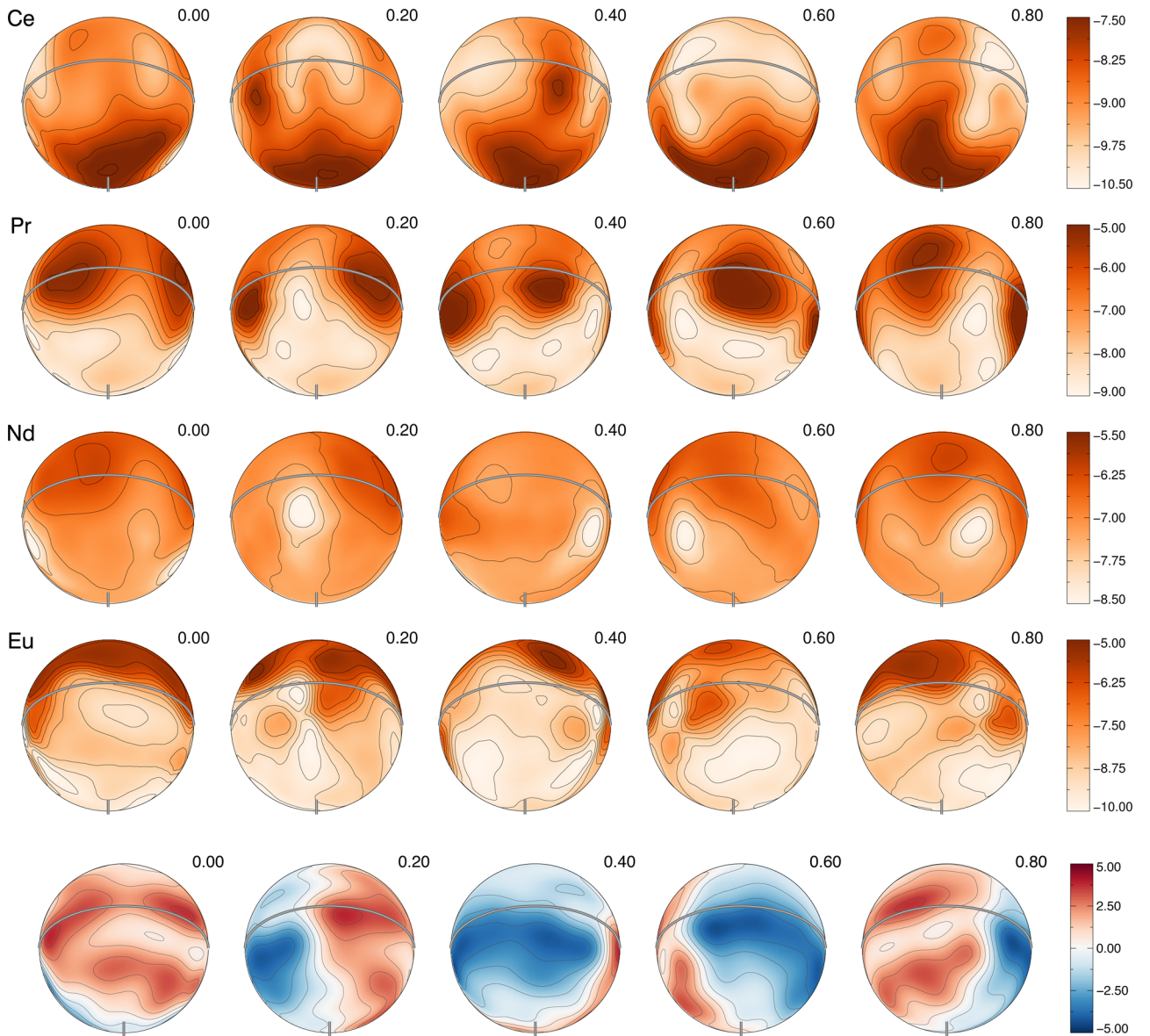


Figure 10. Same as Fig. 9 but for the abundance distributions of Ce, Pr, Nd and Eu, with the radial magnetic field shown in the bottom row.

(1994), who used broad-band linear polarization measurements to model the magnetic field of 49 Cam, concluding that 49 Cam had a magnetic structure that departs noticeably from the customary dipole configuration.

Being a cool Ap star, 49 Cam thus contradicts the marginal trend that has been seen in previous studies, in which simpler magnetic field configurations have been found in cooler Ap stars and complex fields have been typically limited to hotter stars. This suggests that stellar effective temperature may not be correlated with the magnetic field complexity in any meaningful way. It is still possible that the field complexity correlates with the stellar age. However, all four Stokes parameter MDI targets are field stars for which age determination is notoriously uncertain (Landstreet et al. 2007).

We find no clear correlations between the abundance distributions of Ca, Ti, Cr and Ce and the magnetic field structure. For the remaining chemical elements, we find two distinct patterns. For Fe, Pr, Nd and Eu, we find that the areas of relative overabundance are localized to the surface zones where the radial magnetic field

is relatively strong and the areas of relative depletion are located where the horizontal magnetic component is strongest. A reverse trend is seen for Sc, with the areas of relative enhancements located where the horizontal field is strong.

Comparing these results to the abundance maps obtained in the studies of α^2 CVn and HD 32633 (Silvester et al. 2014b, 2015), there is a somewhat limited overlap of the elements that were mapped in all three stars and that also show correlations with the magnetic field structure. In the case of α^2 CVn, the elements Fe, Pr, Nd and Eu show correlations with the magnetic field and in fact these correlations agree with those found for 49 Cam, with these elements being relatively overabundant in the areas of higher radial magnetic field and depleted at the areas near the magnetic equator or stronger horizontal field component. In the case of HD 32633, only the elements Fe and Nd show clear correlations with the field. For Nd, we see similar behaviour with an enhancement in the regions of stronger radial magnetic field component. In the case of iron in HD 32633, we find the opposite

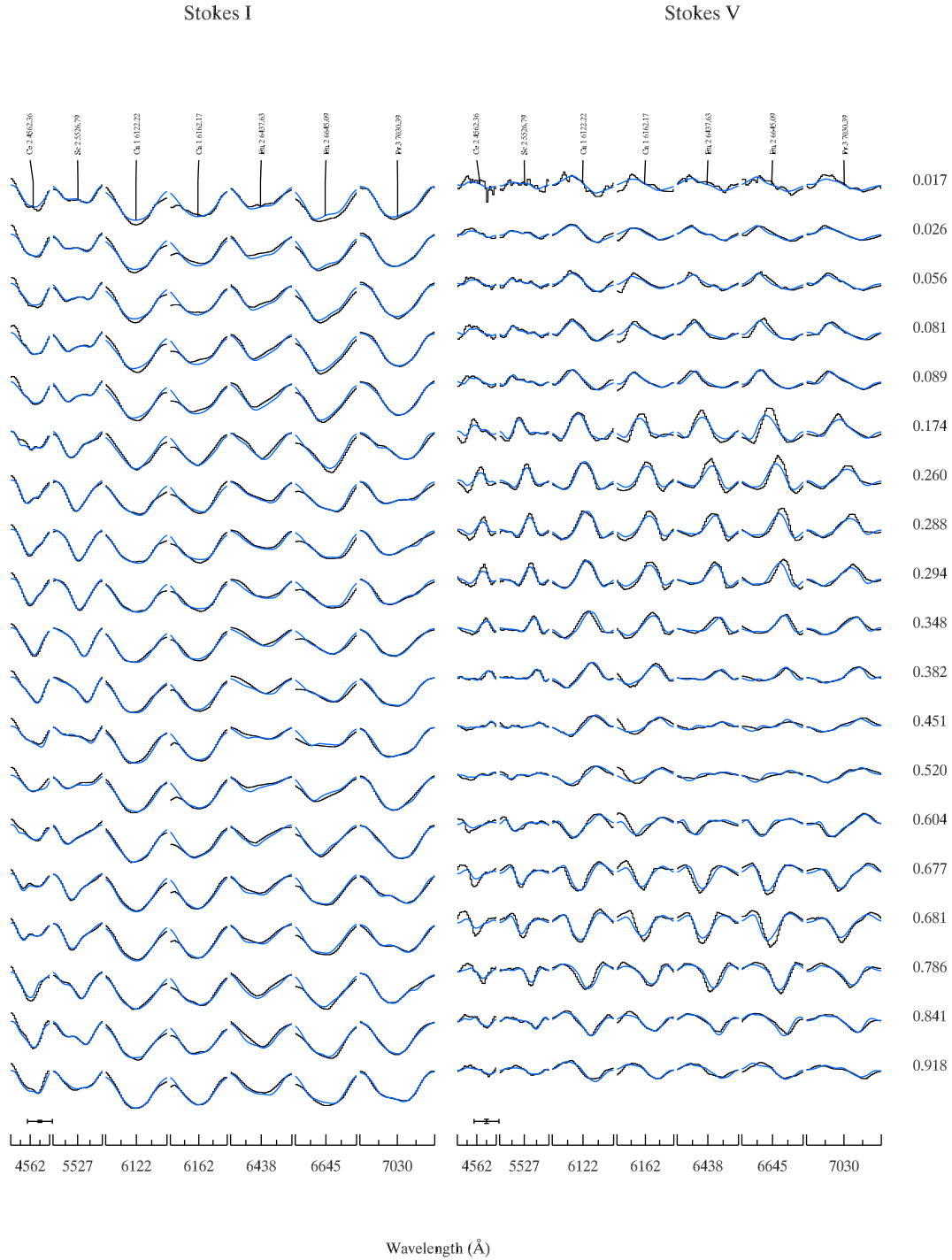


Figure 11. Observed (black histogram line) and synthetic (solid blue line) Stokes *IV* spectra of Ca, Sc, Ce, Pr and Eu lines used for the abundance mapping of these elements.

behaviour, with the areas of enhancement located near the magnetic equator.

Considering our abundance mapping results in the light of theoretical radiative diffusion predictions by Alecian (2015), there is only one element, iron, for which we find clear correlations with the magnetic field structure and that has been studied in this theoretical work. The theory predicts that the abundance enhancement must appear as a ring-like structure at the magnetic equator. Whilst in our maps of 49 Cam we find iron is indeed distributed in a ring-like structure, instead of being located on the magnetic equator as

predicted by theory, we find the ring to be located in the areas of strong radial magnetic field, and this ring is broken near the magnetic equator. On the other hand, our observations do support the prediction by Michaud, Charland & Megessier (1981), who suggested iron to be enhanced where the field is vertical.

It is worth noting that the Ap stars mapped recently have shown a variety of magnetic field substructures, with levels of complexity differing between stars. Perhaps with Ap/Bp stars showing this magnetic diversity (at least in the small-scale magnetic field or in the higher order harmonic modes), the comparison of observed

abundance structures to theoretical models based on simplified models of the magnetic field is not advisable.

We suggest that, when assessing the agreement between the theoretically predicted and observed abundance structures, theoretical modelling should be done on star-by-star basis, taking into account the individual, often complex stellar magnetic field topologies. Just as early models of the magnetic field geometry of Ap/Bp stars assumed a simple dipolar structure, we now understand through advances in instrumentation and modelling techniques how complex these magnetic fields actually are.

ACKNOWLEDGEMENTS

OK acknowledges the financial support from the Knut and Alice Wallenberg Foundation, the Swedish Research Council and the Swedish National Space Board. GAW acknowledges Discovery Grant support from the Natural Sciences and Engineering Research Council (NSERC) of Canada. This work was based on observations obtained at the Canada–France–Hawaii Telescope (CFHT), which is operated by the National Research Council of Canada, the Institut National des Sciences de l'Univers of the Centre National de la Recherche Scientifique of France and the University of Hawaii, and also based on observations obtained at the Bernard Lyot Telescope (TBL, Pic du Midi, France) of the Midi-Pyrénées Observatory, which is operated by the Institut National des Sciences de l'Univers of the Centre National de la Recherche Scientifique of France.

REFERENCES

- Adelman S. J., 1982, *A&AS*, 49, 663
 Adelman S. J., 1997, *A&AS*, 122, 249
 Adelman S. J., Pyper D. M., Shore S. N., White R. E., Warren W. H., Jr, 1989, *A&AS*, 81, 221
 Alecian G., 2015, *MNRAS*, 454, 3143
 Babel J., 1994, *A&A*, 283, 189
 Bessell M. S., Castelli F., Plez B., 1998, *A&A*, 333, 231
 Bonsack W. K., Pilachowski C. A., Wolff S. C., 1974, *ApJ*, 187, 265
 Braithwaite J., Nordlund Å., 2006, *A&A*, 450, 1077
 Cohen M., Wheaton W. A., Megeath S. T., 2003, *AJ*, 126, 1090
 Cowley A. P., 1968, *PASP*, 80, 453
 Duez V., Mathis S., 2010, *A&A*, 517, A58
 Duez V., Braithwaite J., Mathis S., 2010, *ApJ*, 724, L34
 Glagolevskij Y. V., 2011, *Astrophysical Bulletin*, 66, 144
 Khan S. A., Shulyak D. V., 2006, *A&A*, 448, 1153
 Kochukhov O., 2016, in Rozelot J.-P., Neiner C., eds, *Lecture Notes in Physics*, Vol. 914, *Cartography of the Sun and the Stars*. Springer International Publishing, Switzerland, p. 177
 Kochukhov O., 2017, *A&A*, 597, A58
 Kochukhov O., Bagnulo S., 2006, *A&A*, 450, 763
 Kochukhov O., Piskunov N., 2002, *A&A*, 388, 868
 Kochukhov O., Wade G. A., 2010, *A&A*, 513, A13
 Kochukhov O., Drake N. A., Piskunov N., de la Reza R., 2004, *A&A*, 424, 935
 Kochukhov O., Makaganiuk V., Piskunov N., 2010, *A&A*, 524, A5
 MiMeS Collaboration Kochukhov O., Lüftinger T., Neiner C., Alecian E., 2014, *A&A*, 565, A83
 Landstreet J. D., Bagnulo S., Andretta V., Fossati L., Mason E., Silaj J., Wade G. A., 2007, *A&A*, 470, 685
 Leone F., Catanzaro G., Catalano S., 2000a, *A&A*, 355, 315
 Leone F., Catanzaro G., Catalano S., 2000b, *A&A*, 355, 315
 Leroy J. L., Landstreet J. D., Bagnulo S., 1994, *A&A*, 284, 491
 Leroy J. L., Landolfi M., Landi Degl'Innocenti E., 1996, *A&A*, 311, 513
 Lipski Ł., Stepień K., 2008, *MNRAS*, 385, 481
 Michaud G., Charland Y., Megessier C., 1981, *A&A*, 103, 244
 Michaud C., Alecian G., Richer J., 2015, *Atomic Diffusion in Stars*. Springer-Verlag, Berlin
 Piskunov N., Kochukhov O., 2002, *A&A*, 381, 736
 Rusomarov N., Kochukhov O., Ryabchikova T., Piskunov N., 2015, *A&A*, 573, A123
 Rusomarov N., Kochukhov O., Ryabchikova T., Ilyin I., 2016, *A&A*, 588, A138
 Ryabchikova T. A., Savanov I. S., Malanushenko V. P., Kudryavtsev D. O., 2001, *Astron. Rep.*, 45, 382
 Ryabchikova T., Piskunov N., Kurucz R. L., Stempels H. C., Heiter U., Pakhomov Y., Barklem P. S., 2015, *Phys. Scr.*, 90, 054005
 Shulyak D., Tsymbal V., Ryabchikova T., Stütz C., Weiss W. W., 2004, *A&A*, 428, 993
 Silvester J., Wade G. A., Kochukhov O., Bagnulo S., Folsom C. P., Hanes D., 2012, *MNRAS*, 426, 1003
 Silvester J., Kochukhov O., Wade G. A., 2014a, *MNRAS*, 440, 182
 Silvester J., Kochukhov O., Wade G. A., 2014b, *MNRAS*, 444, 1442
 Silvester J., Kochukhov O., Wade G. A., 2015, *MNRAS*, 453, 2163
 Stepień K., 1989, *A&A*, 220, 105
 Stibbs D. W. N., 1950, *MNRAS*, 110, 395
 van Leeuwen F., 2007, *A&A*, 474, 653
 Wade G. A., Donati J.-F., Landstreet J. D., Shorlin S. L. S., 2000, *MNRAS*, 313, 823

This paper has been typeset from a $\text{\TeX}/\text{\LaTeX}$ file prepared by the author.